JOURNAL OF GEOPHYSICAL RESEARCH, VOL. 115, C04014, doi:10.1029/2009JC005558, 2010

An analysis of the effects of swell and surface roughness spectra on microwave backscatter from the ocean

Paul A. Hwang[1] and William J. Plant[2]

Received 4 June 2009; revised 9 November 2009; accepted 16 November 2009; published 9 April 2010.

[1] The spectrum of ocean surface roughness is significantly modified by the presence of background long waves not generated by local wind. Active radar scattering and passive microwave emission from the ocean surface are therefore modified by swell conditions. Here we investigate predictions of the normalized radar cross section (NRCS) of the sea by a multiscale radar scattering model using four different spectral functions, one of which accounts for swell effects. Variations in predicted NRCS using the different spectral functions are quantified. As a result, the effect of swell on microwave backscatter can be separated from uncertainty due to the form of the spectrum without swell. The tilting effects of swell are also examined, and their effect on backscatter is calculated using the model. We find that changes in the ocean surface roughness spectrum due to swell reduce the wind speed dependence of the NRCS at low and moderate incidence angles while tilting effects produce changes in both the incidence angle and wind speed behavior of the NRCS. In general C band NRCS measurements are better explained by the multiscale model and less sensitive to choice of roughness spectral model than are Ku band NRCS values.

Citation: Hwang, P. A., and W. J. Plant (2010), An analysis of the effects of swell and surface roughness spectra on microwave backscatter from the ocean, *J. Geophys. Res.*, *115*, C04014, doi:10.1029/2009JC005558.

1. Introduction

[2] Radar backscatter from the ocean surface has been used very effectively for retrieving wind velocity vectors from the global oceans. The success illustrates the close correlation between radar scatter from the ocean surface and ocean surface roughness, as well as the dominance of wind-generated waves relevant to radar backscatter. Despite this successful application of ocean remote sensing, our understanding of the surface wave properties in the short and intermediate scales remains rather unsatisfactory. For example, several wave spectral models widely employed by different groups of researchers and claimed to yield good normalized radar cross-section (NRCS or σ_o) values in comparison to field measurements are in fact different from each other in significant ways. In section 2, four spectral functions from three spectral models [*Plant*, 2002; *Elfouhaily et al.*, 1997; *Hwang*, 2008] are examined. Field measurements of filtered mean square slopes (MSS) reported in the literature are compared with the MSS integrated from these roughness spectral models. The MSS data sets include Sun glitter (optical) measurements of *Cox and Munk* [1954] in clean and slick waters, and radar data at Ka band (36 GHz, cutoff surface wave number 162 rad/m) by *Walsh et al.* [1998] and *Vandemark et al.* [2004], Ku band (13.6 GHz, cutoff surface wave number about 63 rad/m) by *Jackson et al.* [1992] (including measurements by *Jones et al.* [1977] and *Wentz* [1977]), and C band (5.35 GHz, cutoff surface wave number 24 rad/m) by *Hauser et al.* [2008].

[3] The four spectral functions are used as input for the computation of NRCS values using the stochastic, multiscale model of *Plant* [2002]. The results are compared with several geophysical model functions (Ku band, SASS2 [*Wentz et al.*, 1984] and Ku2001 (the lookup table of Ku2001 (~50 Mb) was downloaded from ftp.ssmi.com with permission provided by D. Smith (personal communication, 2009)); C band, CMOD4 [*Stoffelen and Anderson*, 1997] and CMOD5 [*Hersbach et al.*, 2007]), as well as field data sets covering 1–18 GHz radar frequencies [*Unal et al.*, 1991; *Plant*, 2002; *Mouche et al.*, 2005]. The impact of swell on the NRCS is discernable based on the analysis of these comparison results (section 3). Section 4 is a summary.

2. A Brief Comparison of Roughness Spectral Models

[4] As mentioned in section 1, four spectral functions from three spectral models are used in the NRCS computations in this paper. For convenience, the three spectral models are denoted as D (Donelan-Banner-Plant), E (Elfouhaily et al.) and H (Hwang) spectra. The details of the spectral models have been described by *Donelan et al.* [1985], *Banner* [1990], *Plant* [2002], *Elfouhaily et al.* [1997] and *Hwang* [2008], respectively, and will not be repeated here. In an earlier study, *Plant* [2002] found that for the D spectrum, it is

[1]Remote Sensing Division, Naval Research Laboratory, Washington, D. C., USA.

[2]Applied Physics Laboratory, University of Washington, Seattle, Washington, USA.

0148-0227/10/2009JC005558

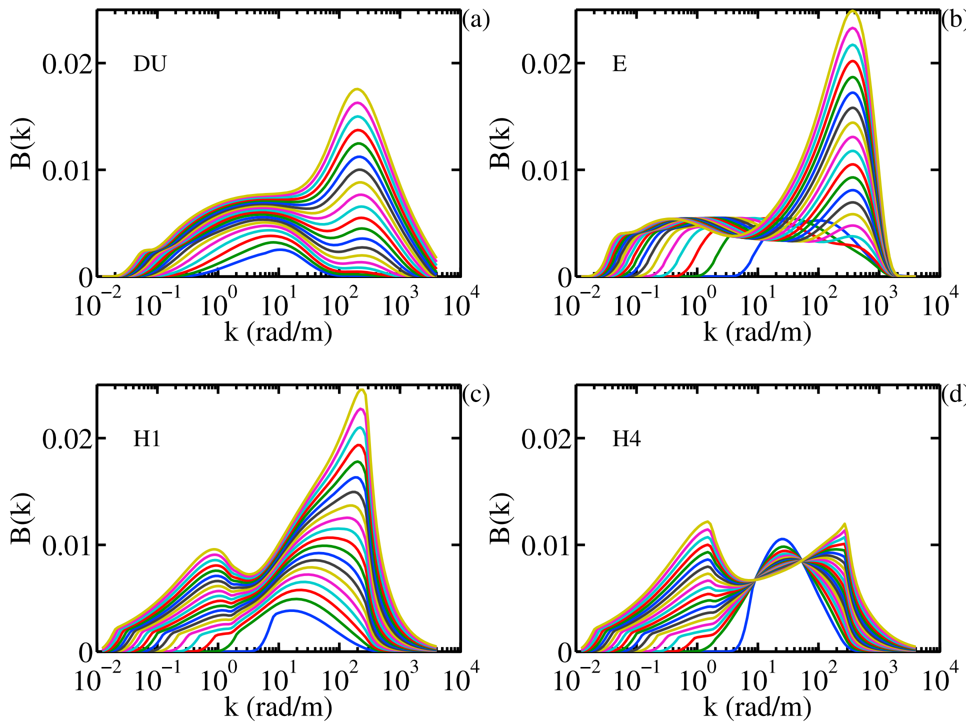

Figure 1. Azimuthally integrated ocean surface roughness spectra, $B(k)$: (a) DU spectrum (Donelan-Banner-Plant with wind speed fluctuation of 1.5 m/s standard deviation) [*Plant*, 2002], (b) E spectrum [*Elfouhaily et al.*, 1997], (c) H1 spectrum [*Hwang*, 2008] (wind sea), and (d) H4 spectrum [*Hwang*, 2008] (strong swell). Wind speed increases upward from 1 to 20 m/s in 1 m/s steps.

important to incorporate wind speed fluctuation in the spectral computation at low wind condition in order to produce reasonable NRCS values at wind speeds below 3 m/s; a wind speed standard deviation of 1.5 m/s was suggested. The D spectrum with 1.5 m/s wind fluctuations is denoted as the DU spectrum in the following. From numerical experiments, incorporating wind speed fluctuations is much less critical to the scattering computation using the E and H spectra, presumably because the empirical nature of these spectral models that already have the wind speed fluctuation built in the data used in formulating the parameterization functions. The H spectrum is also a function of swell intensity, expressed as a swell index quantifying the relative spectral densities between low- and high-frequency bands (with respect to a reference frequency defined by wind speed and measured spectral peak frequency). *Hwang* [2008] provided parameterization functions for four levels (1–4) of swell index, with level 1 corresponding to mostly wind sea in the field and 4 the highest swell influence in the data available for the spectral parameterization. In the following, H1 to H4 denotes the H spectrum with swell index 1–4. For clarity of presentation, only results of H1 and H4 are given.

[5] Figure 1 displays the DU, E, H1 and H4 azimuthally integrated curvature spectra $B(k)$ (equals k^4 times height spectra) for wind speeds from 1 to 20 m/s in 1 m/s steps. We will call this the surface roughness spectrum. (Note, the swell index is quantified by the ratio of the spectral densities in the frequency bands $\omega < 0.6\omega_r$ and $\omega \geq 0.6\omega_r$, the reference frequency ω_r is the higher value between the measured spectral peak frequency, ω_p, and the analytical peak frequency of a fully developed sea defined as $\omega_0 = g/(1.2U_{10})$. Also, as explained in section 5.1 of *Hwang* [2008, p. 11], "During a few of the deployments, the compass orientation was not aligned properly and the swell directional information becomes unusable in the assembled data set." It is unfortunate that we are unable to discuss the directional aspect of the observed decrease of spectral density in H4 compared to H1.) The semilogarithmic plot of the dimensionless spectrum as a function of wave number is an area-conserving representation of the MSS of the ocean surface, that is, the area under the curve of a given wave number range is the filtered MSS of the identified wave number components.

[6] Similarities and differences in the spectral distributions of the ocean surface roughness between these spectral models are conspicuous. Several notable points include the following.

[7] 1. In wind sea condition, all models suggest that the dominant contribution of surface MSS comes from short- and intermediate-scale surface waves from roughly 1 cm to 20 m long.

[8] 2. In the absence of swell, all roughness spectra exhibit peaks near 2–3 cm and a rapid dropoff in the capillary wave region. Waves in this spectral peak wavelength range are too long to be parasitic capillary waves but could be surface roughness produced by breaking waves.

[9] 3. With strong swell (H4 spectrum), short waves in the above mentioned spectral peak range and slightly longer are significantly suppressed. The spectral density in the region

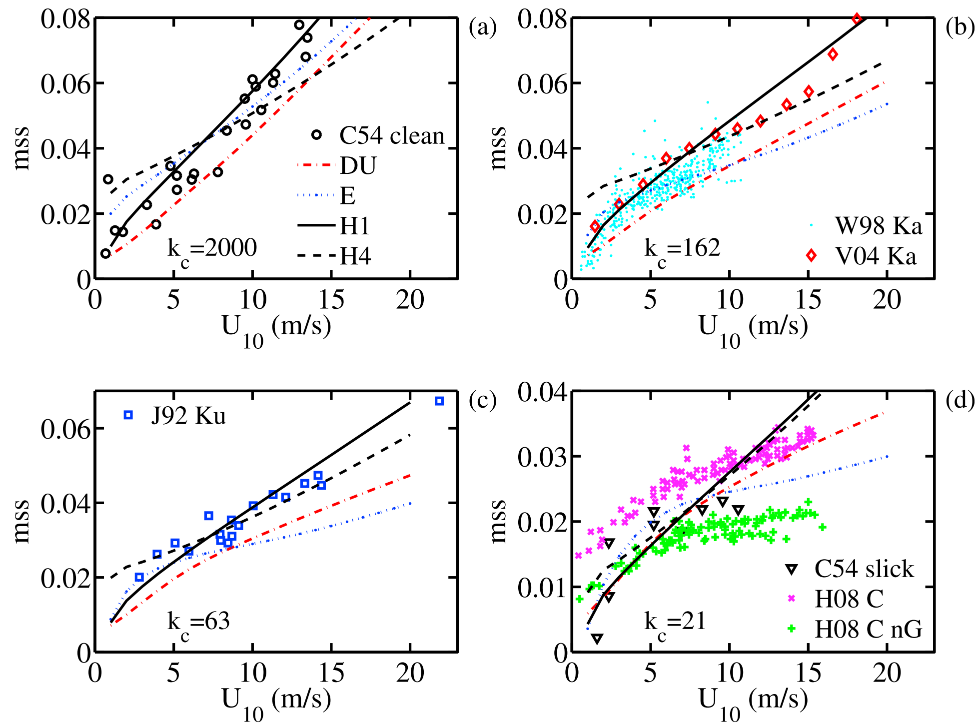

Figure 2. Mean square slopes obtained by integrating the DU, E, H1, and H4 spectral functions from the spectral peak wave number to an upper cutoff wave number, k_c, and their comparison with field data: (a) k_c = 2000 rad/m and clean water Sun glitter data of *Cox and Munk* [1954], (b) k_c = 162 rad/m and Ka band radar data of *Walsh et al.* [1998] and *Vandemark et al.* [2004], (c) k_c = 63 rad/m and Ku band radar data of *Jackson et al.* [1992] (including data of *Jones et al.* [1977] and *Wentz* [1977]), and (d) k_c = 21 rad/m and slick water Sun glitter data of *Cox and Munk* [1954] and C band radar data of *Hauser et al.* [2008].

is much less sensitive to wind speed and, in fact, decreases slightly with increasing wind for waves with wavelengths between about 9 and 90 cm.

[10] 4. The spectral peaks of $B(k)$ in the four spectral functions behave differently. As wind speed increases, the DU peaks move slightly toward lower k, the E peaks remain at almost constant k, and H1 peaks move toward higher k.

[11] 5. All spectral functions display a bimodal appearance with two separate local peaks in the high and low wave numbers as wind speed increases. The weighting of roughness spectral density is much larger in the high wave number peak for wind seas. The suppression of decimeter-scale waves by swell causes the H4 spectrum to reverse the weighting of the two local peaks.

[12] The observation of decreased wind sensitivity of decimeter-scale waves due to swell influence as described in the third point is of special interest. Relevant investigations of wave breaking from radar sea spike analysis [*Hwang et al.*, 2008a, 2008b] and energy dissipation consideration [*Hwang*, 2009a] indicate that the dominant velocity scale of wave breaking is in the neighborhood of 1.5–3 m/s or wavelength scale 1.5–6 m (k between about 1 and 4 rad/m). Field observations further show that the length scale of breaking becomes shorter in the presence of swell [*Hwang and Wang,* 2004; *Hwang et al.*, 2008b], possibly due to orbital modulation producing premature breaking of short-scale waves. Because wave breaking is in fact an important generation source of short-scale surface roughness [*Hwang*, 2007], this relatively narrow band of breaking wavelength scale may explain partially the wind speed insensitivity of decimeter- to meter-scale waves in the roughness spectrum, especially in swell dominant condition.

[13] With the wave spectral functions, the MSS integrated over a given wave number range can be carried out. The integrated MSS can be compared with those measured by remote sensing techniques with different EM frequencies. There are now several large data sets reported in the literature that resolve a broad range of wind and wave coverage. The cutoff wave number varies from essentially infinite for optical measurements (including clean water and natural or artificial slicks) [*Cox and Munk*, 1954] to short gravity wave components at radar frequencies of Ka (36 GHz) [*Walsh et al.*, 1998; *Vandemark et al.*, 2004], Ku (14 GHz) [*Jackson et al.*, 1992] (including data by *Jones et al.* [1977] and *Wentz* [1977]) and C band (5.35 GHz) [*Hauser et al.*, 2008] in an altimeter mode of operation. Figure 2 displays a comparison of these remote sensing measurements with the integrated MSS from the spectral models mentioned above. The cutoff wave number of C band (24 rad/m) and slick cases (21 rad/m) are very similar and the data are grouped together in Figure 2d. The analyses of *Hauser et al.* [2008] produce two sets of MSS with assumptions of Gaussian (shown by *Hauser et al.* [2008, Figure 5d]) and non-Gaussian [*Hauser et al.* [2008, Figure 11b] surface

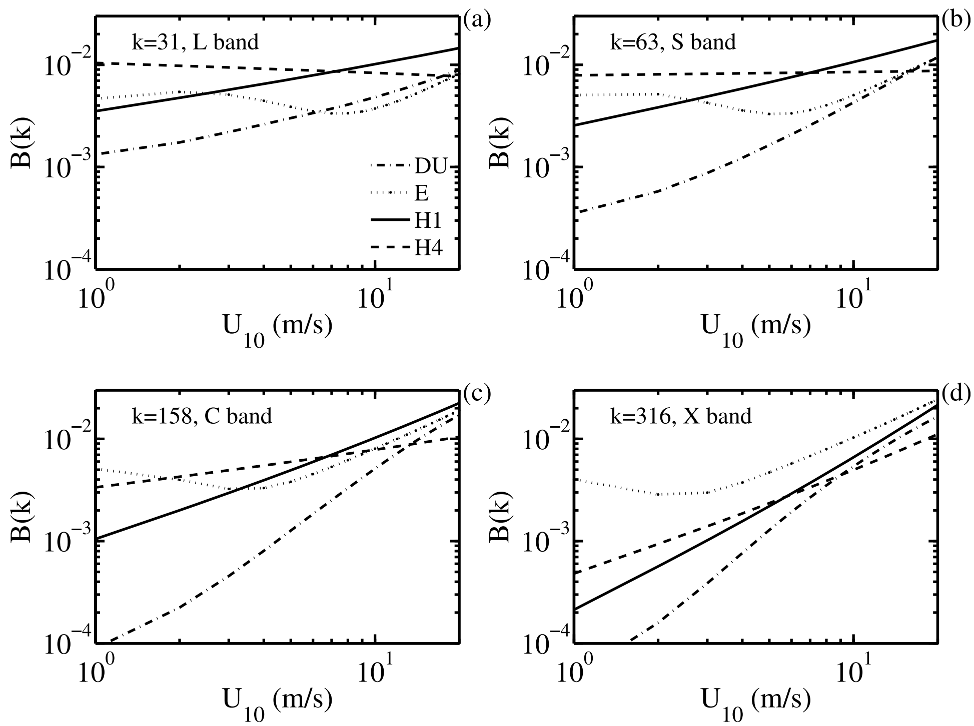

Figure 3. Dimensionless spectral densities of representative Bragg wave components at several radar frequencies (k = 31, 63, 158, and 316 rad/m, corresponding to Bragg wavelengths at radar frequencies at about L, S, C, and X bands) calculated with DU, E, H1, and H4 spectral functions.

slope probability density function; both reported C band MSS sets are included in Figure 2d. The DU spectrum yields good agreement with MSS for low k_c but somewhat underpredicts the MSS for higher k_c. The E spectrum produces good agreement for both high and low ends of the k_c range but underpredicts the intermediate k_c for wind speed higher than about 7 m/s. Overall, the H spectrum (with H1 and H4 forming the approximate envelop of expected MSS range) seems to provide an overall better agreement with the collected data sets but the wind speed dependence for the lowest k_c differs considerably from the data trend (Figure 2d). However, MSS measurements at low k_c in the open ocean are frequently contaminated by background swell and retrieval of their wind speed dependence is a challenging task, as discussed in more detail by *Hwang* [2008, 2009b]. Comparing the H1 and H4 curves for all cutoff wave number cases, in the presence of swell (H4) the wind speed dependence decreases considerably, as would be expected from the mixture of contributions from local wind generation and nonlocal swell sources.

[14] For airborne or spaceborne applications with moderate radar incident angles, say from 25° to 55°, Bragg scattering is generally the most important mechanism of radar return from the ocean surface [e.g., *Wright*, 1966, 1968; *Bass et al.*, 1968; *Valenzuela,* 1968, 1978; *Plant*, 2002]. The behavior of the Bragg wave as a function of wind condition is thus of great interest for wind speed retrieval using the scatterometer data. Figure 3 shows the wind speed dependence of the curvature spectrum at k = 31, 63, 158 and 316 rad/m, corresponding to Bragg wavelengths at radar frequencies of about L, S, C and X bands. Both the magnitude of the spectral densities and the wind speed dependence in the four spectral functions differ considerably. Particularly, the nonmonotonic wind speed dependence in the E spectrum is quite different from the other models and our experience of wind speed dependence of surface wave growth. In general, the wind speed dependence becomes weaker as radar wavelength increases. At L and S bands, the presence of strong swell may wipe out the wind speed signal in the Bragg component and only the tilting effect provides the wind speed dependence of the radar return according to the H4 spectral function.

3. NRCS Comparisons

3.1. Frequency Dependence

[15] Many NRCS measurements at various microwave frequencies have been reported. Early data, such as the four frequency measurements by NRL scientists in the 1970s, generally suffer from problems of absolute calibration and less detail in associated ocean wind and wave information. *Unal et al.* [1991] present field measurement of radar cross section at 1.2, 3.2, 5.3, 13.7 and 17.25 GHz over the Atlantic Ocean close to Bretagne, France at the end of autumn 1987 (from 17 November to 4 December). Their results for the azimuthally averaged NRCS and polarization ratio, $\sigma_o(VV)/\sigma_o(HH)$, at 10 m/s wind speed for three incident angles (20°, 30° and 45°) are given in Figures 4 and 5. These data and the geophysical model functions (GMF) CMOD4 for C band VV and NSCAT2 for Ku band VV and HH are used by *Plant* [2002] to compare with his model results using the DU and E spectra. Here, compu-

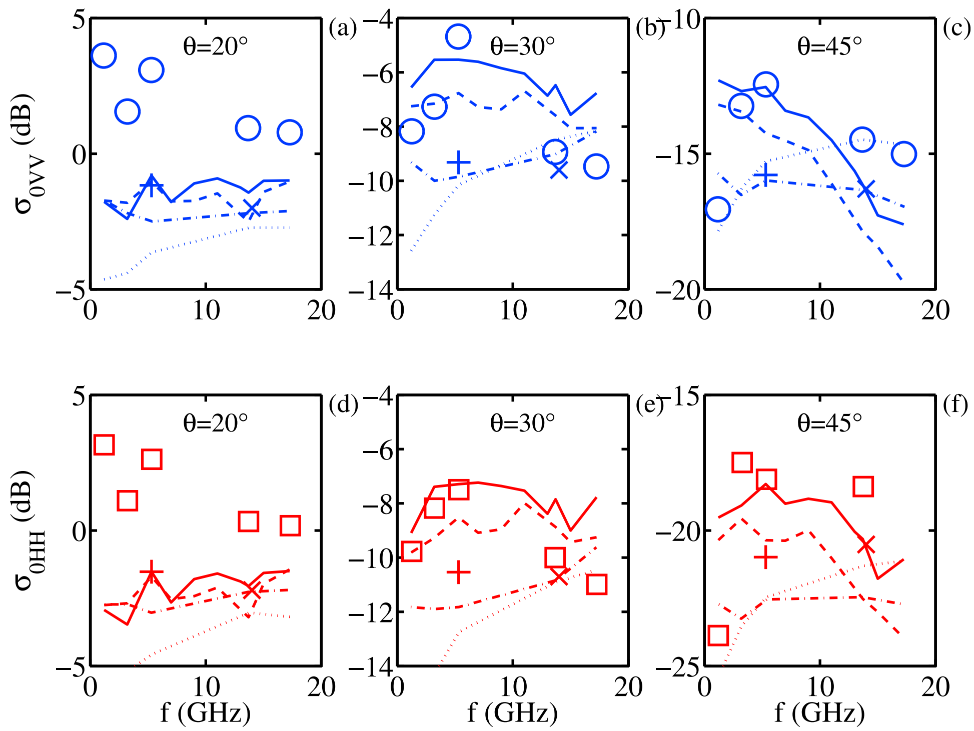

Figure 4. Calculated azimuthally averaged NRCS values ((a, b, c) for VV and (d, e, f) for HH at 20°, 30°, and 45° incidence angles) at different radar frequencies compared with measurements by *Unal et al.* [1991] and scatterometer geophysical model functions. Key is circle, measured VV; square, measured HH; plus, CMOD4; cross, SASS2; dash-dotted curve, DU spectrum; dotted curve, E spectrum; solid curve, H1 spectrum; and dashed curve, H4 spectrum. The wind speed is 10 m/s.

tations using the H1 and H4 spectra as input to Plant's multiscale radar scatter model are also included in the comparison. In Figures 4 and 5, the dash-dotted, dotted, solid, and dashed curves show results using the DU, E, H1 and H4 spectra, respectively. The azimuthally averaged NRCS for the three incident angles are shown in Figure 4 (VV in Figures 4a–4c and HH in Figures 4d–4f). The circle and square markers represent data [*Unal et al.*, 1991] while GMF are shown as plusses for CMOD4 and crosses for SASS2; more discussion on the comparison with GMF is given in section 3.2. The VV to HH ratio is shown in Figure 5, where circle, square and pentagram are for data at 20°, 30° and 45°, respectively. The corresponding NRCS computations using DU, E, H1 and H4 spectra are given in the same color as the data for each incidence angle. As noticed by *Plant* [2002], the model predictions using DU and E spectra are generally somewhat below the data of Unal et al. but closer to the values obtained from the GMF. The NRCS computations using the H1 and H4 spectra generally improve the agreement with Unal et al.'s data at the higher incidence angles but reduce the agreement with the GMF. *Plant* [2002] also commented that the VV to HH polarization ratio predicted by the multiscale model using DU and E spectra at 45° incidence angle is larger than either the data of Unal et al. or those given by the GMF (Figure 5). He considered that to be a common feature of composite Bragg surface scattering models. The VV/HH ratio of backscatter computed with H spectra at 45°, however, is in very good agreement with Unal et al. data and the GMF.

3.2. Ku Band and C Band Comparisons

[16] In concert with satellite missions of wind measurements, a large volume of airborne and spaceborne NRCS data at Ku and C band frequencies have been analyzed in

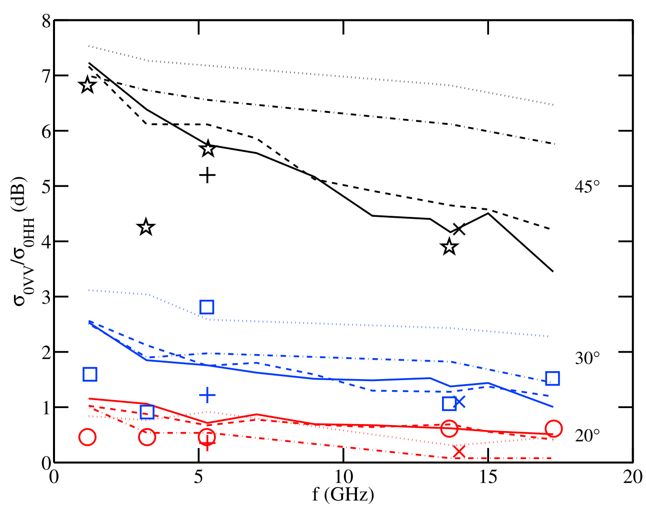

Figure 5. Same as Figure 4 but for the VV/HH ratio. Symbols are as follows: circle, square, and star are measurements at θ = 20°, 30°, and 45°, respectively; plus is CMOD4; and cross is SASS2. Curve types for the different spectral functions are the same as those in Figure 4. Results for the same incident angle are shown in the same color.

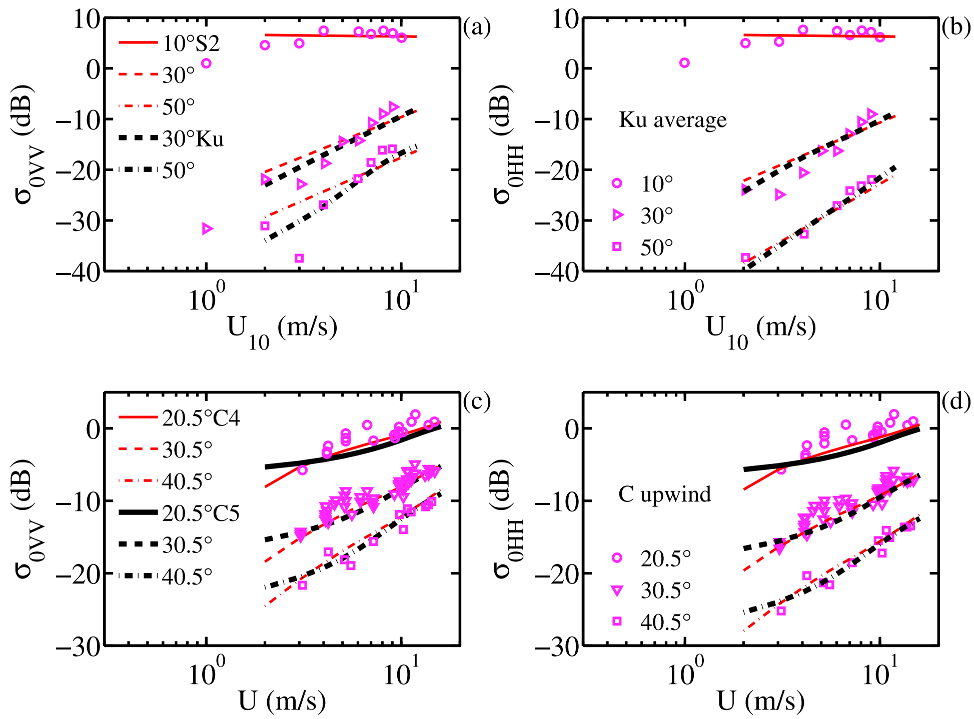

Figure 6. Comparison of GMF (SASS2 and Ku2001 for Ku band and CMOD4 and CMOD5 for C band) with field measurements by airborne radars (Ku band [*Plant*, 2002] and C band [*Mouche et al.*, 2005]). (a) Ku band directional average, vertical polarization; (b) Ku band directional average, horizontal polarization; (c) C band upwind, vertical polarization; and (d) C band upwind, horizontal polarization. Abbreviations used in the legend are S2, SASS2; Ku, Ku2001; C4, CMOD4; and C5, CMOD5.

considerable detail. These data are used to establish the GMF for extraction of wind velocity vectors from satellite radar measurements. Figures 6a and 6b show an example of comparison between airborne Ku band data reported by *Plant* [2002] and two generations of the Ku band GMF (SASS2 [*Wentz et al.*, 1984] and Ku2001 (D. Smith, personal communication, 2009)); Figure 6c shows a similar comparison of airborne C band measurements by *Mouche et al.* [2005] and CMOD4 [*Stoffelen and Anderson*, 1997] and CMOD5 [*Hersbach et al.*, 2007] VV GMF. These are coupled with the C band VV/HH polarization ratio algorithm proposed by *Mouche et al.* [2005] to obtain an HH GMF at C band for comparison with the aircraft data. The agreement between measurements and GMF is usually very good. The NRCS computation using the multiscale model [*Plant*, 2002] with the four roughness spectral functions described in section 3.1 can be compared with the GMF. (NSCAT2 is a predecessor of Ku2001. Both Ku2001 and NSCAT2 GMF are given as lookup tables of $\sigma_{pp}(\theta, U_{10}, \varphi)$, where θ is incidence angle in the range of 16°–66° in 0.5° intervals, U_{10} wind speed from 0 to 70 m/s in 0.2 m/s intervals, φ the azimuthal angle from 0° to 180° in 2° intervals, and *pp* polarization (VV and HH) (D. Smith, personal communication, 2009). Ku2001 and NSCAT2 are very similar and they differ slightly from SASS2. Only Ku2001 results are given here.)

[17] Figure 7 illustrates an example of comparison between the multiscale model predictions (solid curves) and Ku2001 (dashed curves). The results are shown as a function of incidence angle in Figures 7a–7d with wind speed ranging from 3 to 21 m/s in 6 m/s intervals (increasing upward), and as a function of wind speed in Figures 7e–7h with incidence angles ranging from 20° to 60° in 10° intervals (increasing downward). The multiscale model computations with DU, E, H1 and H4 spectra are shown in individual plots and placed side by side for comparison. Similar results for HH, polarization ratio, and crosswind, downwind or other azimuthal angles can also be produced. As can be seen from Figure 7, it is difficult to design a comprehensive yet concise scheme to present the comparison results. Here we attempt to quantify the comparison with Figures 7, 8, 9, 10, 11, 12, 13, and 14 and Tables 1, 2, and 3.

[18] Figures 8–10 show the ratio between multiscale model computations and the Ku2001 GMF (azimuthally averaged NRCS) as functions of incidence angle (Figures 8a–8d, 9a–9d, and 10a–10d) and wind speed (Figures 8e–8h, 9e–9h, and 10e–10h) for VV and HH polarizations and VV/HH polarization ratio. The convention of curve styles is identical in Figures 8–10. For the plots as a function of incidence angle (Figures 8a–8d, 9a–9d, and 10a–10d), wind speeds are 3–21 m/s in 6 m/s steps in the sequence of solid black, solid color, dashed black, and dashed color curves. For the plots as a function of wind speed (Figures 8e–8h, 9e–9h, and 10e–10h), incidence angles are 20°–60° in 10° steps in the sequence of solid black, solid color, dashed black, dashed color, and dash-dotted black curves. A difference of ± 1.5 dB is considered excellent and ± 3 dB good in the following discussion. For reference, the horizontal dashed lines in each plot mark the ± 3 dB boundary.

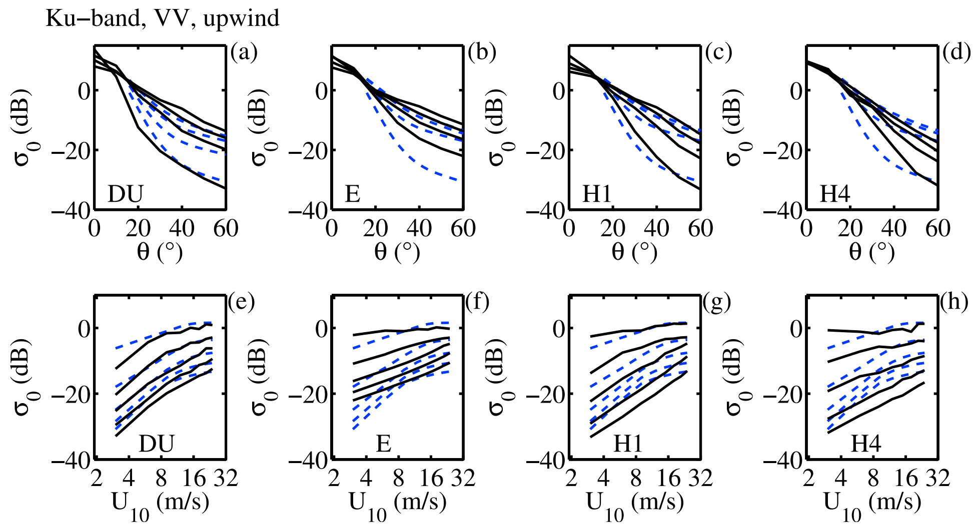

Figure 7. Examples of normalized radar cross sections computed with the multiscale scattering model [*Plant*, 2002] with DU, E, H1, and H4 spectral input (solid curves) and their comparison with Ku2001 model function (dashed curves). (a–d) Results plotted as a function of incidence angle for several wind speeds: U_{10} = 3–21 m/s in 6 m/s steps. (e–h) Results plotted as a function of wind speed for θ = 20°–60° in 10° steps.

[19] For VV polarization (Figure 8), the DU spectrum yields excellent results except at the lower incidence angles of the lowest wind speed condition. The E spectrum yields larger deviation at low wind with increasingly better performance toward high wind. The H1 spectrum (wind sea) achieves reasonably good agreement at low to moderate incidence angles at most wind speeds. For the H4 spectrum (strong swell influence), the computed NRCS is considerably higher than the GMF at the lowest wind speed and θ < ~40°, and much lower at high incidence angle and moderate wind speed. The result for HH polarization is shown in Figure 9. The DU, H1 and H4 spectra underpredict NRCS at high incidence angle, the E spectrum overpredict NRCS at low wind speed. The polarization ratio (Figure 10) is well predicted by DU and E spectra for θ < ~40°, and by H1 and H4 spectra for θ < ~50°. To provide a quantitative reference, the average ratio between scatter computation and GMF for U_{10} between 3 and 24 m/s in 3 m/s steps and θ between 20° and 60° in 10° steps is calculated for each wave spectral function for VV, HH and polarization ratio with

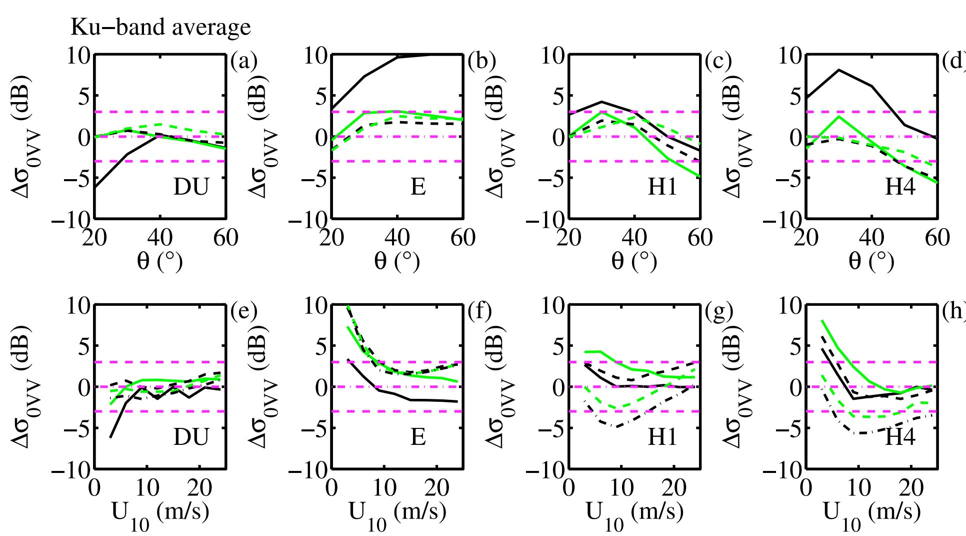

Figure 8. Examples of the cross-section ratio between the multiscale model (with DU, E, H1, and H4 spectral input) and Ku2001 model function (Ku band, 14 GHz) for the azimuthal average VV polarization. (a–d) Results plotted as a function of incidence angle for several wind speeds: U_{10} = 3–21 m/s in 6 m/s steps. (e–h) Results plotted as a function of wind speed for θ = 20°–60° in 10° steps. Curve style sequence for increasing wind speed or incidence angle is black solid, color solid, black dashed, color dashed, and black dash-dotted.

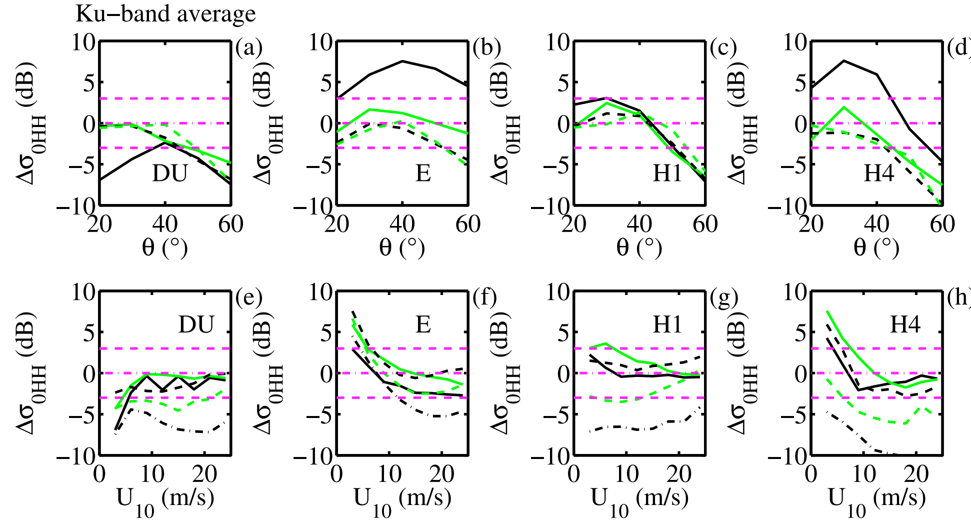

Figure 9. Same as Figure 8 but for HH polarization.

configurations of upwind, crosswind, downwind and azimuthal average. The results (in dB) are listed in Table 1. The percentages of cases with difference within 1.5 and 3 dB are also calculated and listed in Tables 2 and 3, respectively. A summary of Tables 1–3 will be presented after the C band discussion next.

[20] The same sequence of comparisons is carried out for the C band frequency (6 GHz). Figure 11 shows an example of the comparison (VV polarization, upwind) between the calculated NRCS (solid curves), CMOD4 (dashed curves) and CMOD5 GMF (light blue dash-dotted curves) as functions of θ (Figures 11a–11d, wind speed 3–21 m/s in 6 m/s steps, increasing upward) and U_{10} (Figures 11e–11h, incidence angle 20°–60° in 10° steps, increasing downward). The ratio of azimuthally averaged NRCS between scatter computations and CMOD4 is calculated. Figures 12–14 present the result of VV, HH and VV/HH polarization ratio. For C band, the computed azimuthally averaged NRCS is in much better agreement with the model function than the comparison of Ku band. Almost all cases of polarization ratio are within 3 dB difference.

[21] The average ratio and the percentages with difference within 1.5 and 3 dB between scatter computation and GMF for U_{10} between 3 and 24 m/s in 3 m/s steps and θ between 20° and 60° in 10° steps are tabulated in Tables 1–3. Tables 1–3 each contains 12 columns (four columns each for VV, HH and VV/HH) showing the results of upwind, crosswind, downwind and azimuthal average. In each column there are 8 rows for the four different wave spectral functions used; the first four rows are for Ku band and last four are for C band. For convenience, in each column, the best results for the Ku and C bands are in boldface. For the ratio in dB (Table 1), the DU spectrum has the best agreement in Ku band and C band VV polarization and won in three categories (crosswind, downwind and azimuthal average). For HH polarization, the results are more mixed, with H1 performs very well for Ku, and E for C band. In general, the difference between the scatter computation and GMF is

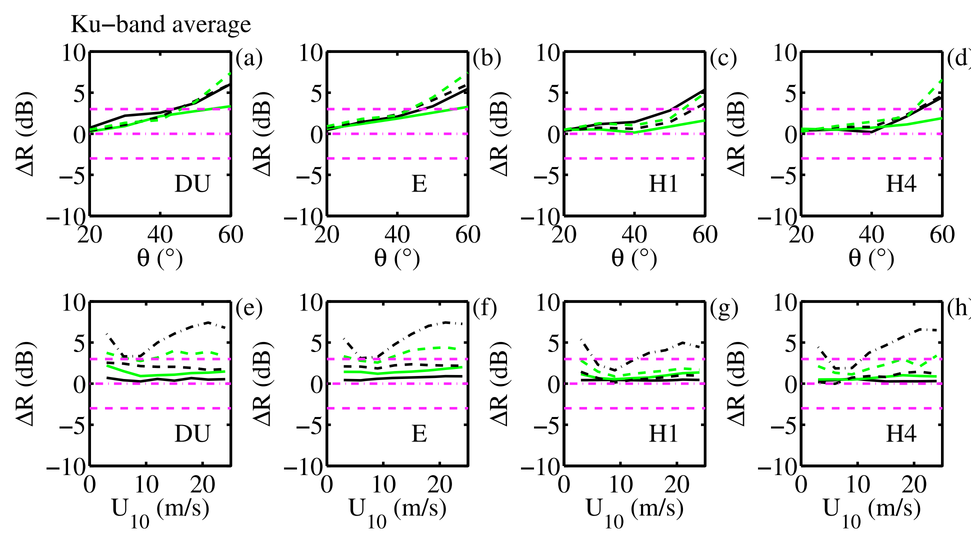

Figure 10. Same as Figure 8 but for VV/HH polarization ratio.

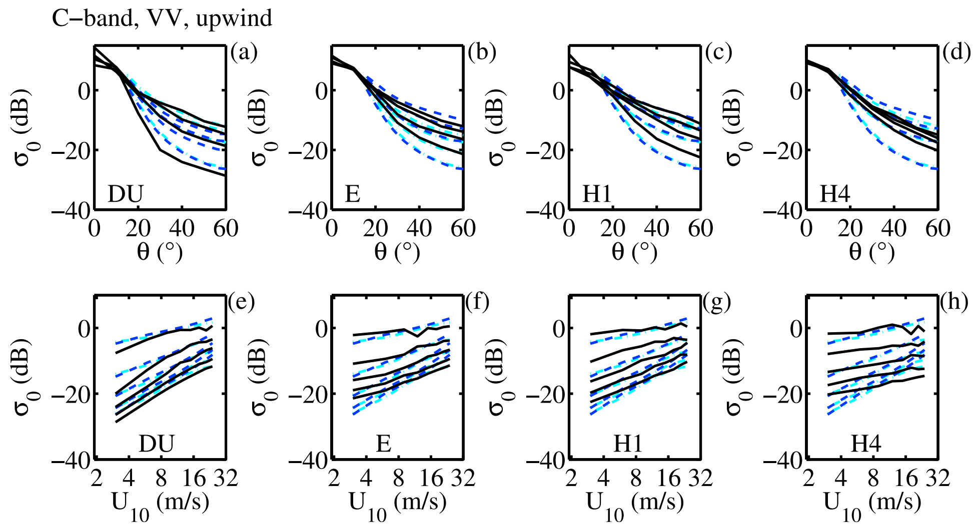

Figure 11. Same as Figure 7 but for C band (dashed curves, CMOD4; light blue dash-dotted curves, CMOD5).

slightly worse for Ku band than for C band. The scatter model performance shows a marked improvement in VV/HH ratio for C band (all spectral models within 1 dB) in comparison to Ku band (varies from 1 to 4 dB). The best VV/HH ratio is with H1 spectrum for Ku band and H4 spectrum for C band. Similar but somewhat more variable conclusions can be drawn for the percentage with a difference less than 1.5 dB (Table 2) or 3 dB (Table 3).

[22] The agreement using DU spectrum is better for VV than HH polarization for Ku band, the result is reversed for E spectrum. Both spectra produce a VV/HH ratio about 3 dB higher than that of GMF (Table 1). Both DU and E spectra obtain better results at C band. H spectra produce more even performance in both VV and HH, as reflected in the better polarization ratio. The average ratios in VV, HH or VV/HH using H1 and H4 spectra are mostly less than 1.5 dB and all less than 3 dB. The VV and HH NRCS calculated with H spectra are worse at C band than Ku band, overestimating the NRCS by 0.92–2.91 dB, or about 1.24–1.95 times larger than the CMOD4 values. This may point toward the need to improve the long wave portion of the H spectral parameterization. The formulation of *Hwang* [2008] assumes fully developed saturation spectrum for waves longer than about 6 m ($k \approx 1$ rad/m).

3.3. Additional Swell Effects

[23] In the computations presented above, the swell effect is only considered through the modification of the roughness spectrum following the empirical result of *Hwang* [2008] but the swell spectral components are not incorporated in the simulated surface wave spectrum. In this portion of the presentation, the swell is represented by a uniformly distributed spectral spike over a rectangular region in wave number and wave direction space. The spectral spike is

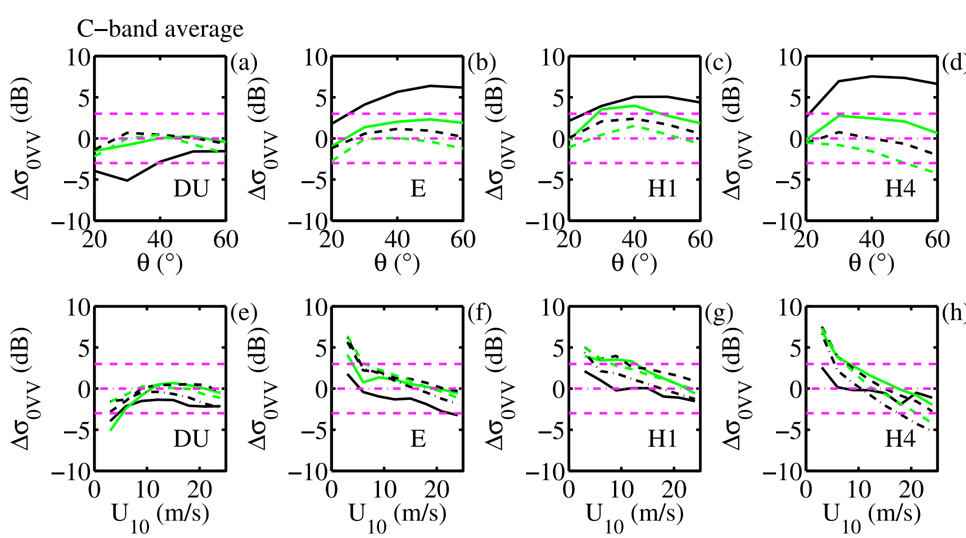

Figure 12. Examples of the cross-section ratio between the multiscale model (with DU, E, H1, and H4 spectral input) and C band CMOD4 GMF for VV polarization.

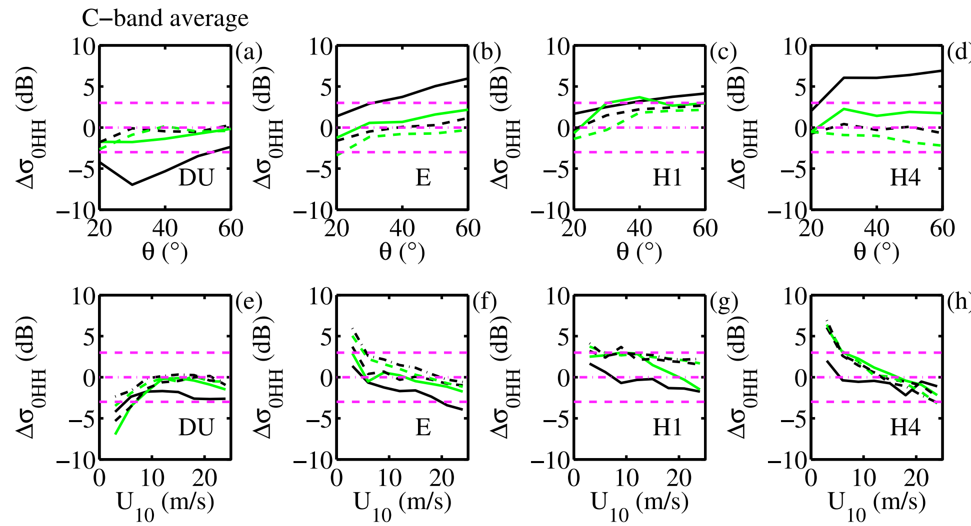

Figure 13. Same as Figure 12 but for HH polarization.

centered at the swell wave number, k_{sw}, and swell direction, φ_{sw}. For simplicity, the swell band width is from 0.5 k_{sw} to 1.5 k_{sw}, and the direction beam width is 14°, which is five directional resolution cells. Due to computational limitations in accommodating very long swell, k_{sw} = 0.1 rad/m is used to demonstrate the swell effect. (In the multiscale scattering model, realizations of the 3-D waveforms of long wave components are generated to produce the tilting surfaces. This step involves numerical operations in 4-D (k_x, k_y, x, y) and puts a practical limitation on resolving small k swell components. From numerical experimentation, using a k_{sw} smaller than 0.1 rad/m frequently puts the swell component into the (0, 0) cell in the (k_x, k_y) domain during the waveform realization process and the swell effect disappears artificially due to the limitation of wave number digitization.) The mean square slope produced by the swell components is 0.01, and the dominant propagation direction is the same as the wind. This is equivalent to a sinusoidal wave train of 63 m long and 1.4 m amplitude.

[24] Figure 15 illustrates the effect on low-incidence-angle backscatter. The result is presented in terms of the NRCS (dB) as a function of $\tan^2\theta$ for the range of incidence angles, θ, from 0° to 16° in 4° steps. In this presentation, the distribution is expected to be linear and the quasi-linear relation is used to infer the ocean surface MSS from radar measurements operated in near-nadir-looking configuration [e.g., *Jackson et al.*, 1992; *Walsh et al.*, 1998; *Hauser et al.*, 2008]. Results from two wind speeds (4 and 16 m/s, with black and pink curves, respectively) are illustrated for demonstration, the connected circles show multiscale model computation for a wind sea while connected squares show results for wind sea plus swell. As illustrated in Figure 15, the swell tilting modifies considerably the slope of the cross-section dependence on incidence angle, $\sigma_0(\tan^2\theta)$, especially for lower wind speed or lower radar frequency because the contribution from swell component becomes relatively more important. Extraction of the wind-

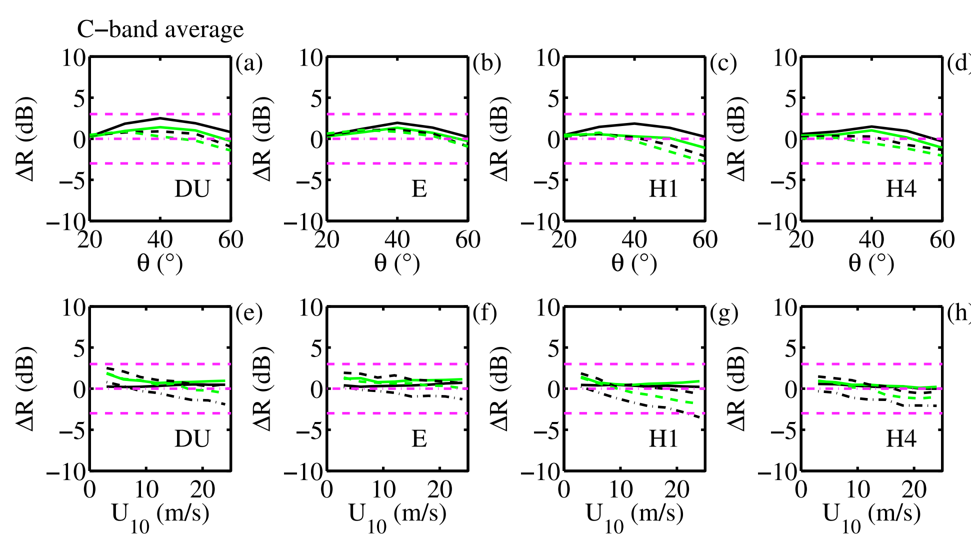

Figure 14. Same as Figure 12 but for VV/HH polarization ratio.

Table 1. Average Ratio Between NRCS Computation and GMF for U_{10} Between 3 and 24 m/s in 3 m/s Steps and θ Between 20° and 60° in 10° Steps[a]

	DVu	DVx	DVd	DVa	DHu	DHx	DHd	DHa	DRu	DRx	DRd	DRa
Ku DU	−0.57	**0.50**	**0.13**	**−0.06**	−2.86	−2.20	−1.60	−2.30	3.05	3.83	2.37	3.09
Ku E	3.01	4.40	3.90	3.66	**0.42**	0.87	2.16	0.98	3.04	4.08	2.42	3.18
Ku H1	0.63	1.06	1.05	0.84	−0.50	**−0.46**	**0.49**	**−0.26**	**1.68**	**2.39**	**1.08**	**1.71**
Ku H4	**0.25**	0.56	0.93	0.49	−0.68	−0.83	0.83	−0.38	2.13	2.82	1.54	2.12
C DU	−1.59	**0.33**	**−0.90**	**−0.83**	−2.13	**−0.04**	−1.08	−1.23	0.68	0.61	0.42	0.57
C E	**0.50**	2.84	1.14	1.39	**−0.17**	2.04	**0.76**	**0.74**	0.59	0.80	0.43	0.62
C H1	1.28	2.89	2.01	1.96	1.16	2.91	2.22	1.97	0.10	0.09	−0.12	**0.01**
C H4	1.28	2.34	1.81	1.72	0.92	2.07	1.62	1.43	**0.02**	**0.06**	**−0.04**	**−0.01**

[a]Average ratio is in dB. Here u, upwind; x, crosswind; d, downwind; a, azimuthal average; R, VV/HH. In each column, the best results for the Ku and C bands are in boldface.

induced ocean surface MSS needs to take into account the effect due to external swell components [*Hwang*, 2009b].

[25] At moderate incidence angles, the swell effect on the backscatter is illustrated in Figure 16 for Ku band and Figure 17 for C band. Experimental data from airborne measurements by *Plant* [2002] and *Mouche et al.* [2005] as well as GMF are also plotted for reference. Radar scatter computation is performed using the H1 and H4 spectra for the incident angles available in the experimental data sets. The results are plotted with and without the swell components using square and circle symbols, respectively. The swell effect is generally less than a few dB, with the magnitude slightly larger in C band than Ku band. The difference is usually larger at lower wind speed because the MSS contribution from swell becomes relatively larger in comparison to the wind generated roughness. A difference between NRCS values calculated with H1 and with H4+sw (H4 plus explicit swell components in simulated input spectrum) of less than about 3 dB is found mostly in VV polarization for $U_{10} \geq \sim 4$ m/s and in HH polarization for $U_{10} \geq \sim 6$ m/s. An exception is found for Ku band HH at $\theta = 50°$ where the H4 NRCS is 6–10 dB higher than the H1 result; interestingly, the NRCS calculated with H4+sw drops back to the H1 level. The abnormal increase is not due to the effect of random phase in the multiscale radar scatter computation since the result is repeatable with additional simulation runs. The cause of the apparently anomalous behavior is not known at this point. The overall results show that for moderate incident angles (20°–50° in the present case), the swell addition tends to cause an increase in H1 NRCS but a decrease in H4 NRCS. These results may help explain the relatively large data scatter in NRCS measurements in the ocean environment.

3.4. Discussion

[26] One of the most importance applications of radar backscatter from the ocean surface is the retrieval of wind velocity from the NRCS. The importance of incorporating swell information into radar scattering problems has been recognized by the altimeter community for some time. *Anderson et al.* [2000] demonstrated the significant improvement of altimeter wind speed retrieval with incorporation of wave height information; a comparison between altimeter derived wind speeds and collocated buoy measurements resulted in a RMS difference of 1.49 m/s and bias 0.50 m/s using a single parameter (σ_0) algorithm, with two parameters (σ_0 and significant wave height, H_s) those statistics improve to 1.23 and 0.035 m/s. Also, the algorithms for correcting the electromagnetic bias in the altimeter sea surface height measurements have advanced from simple wind speed parameterizations to algorithms with wind speed, wave steepness and wave age since the 1990s to improve error statistics by 50 percent [e.g., *Melville et al.*, 1991, 2004]. It seems that the scatterometer wind retrieval can benefit from incorporating wave height and wave period in the retrieval algorithms as well. Admittedly, the scattering mechanisms of radar at moderate incidence angles are more complicated than those of altimeters and the correct specification of ocean surface roughness spectrum is more critical for non-nadir-looking applications than for altimeters. To further complicate the situation, a similar level of increased data spread due to swell as shown in the simulation works here may also be caused by wind speed fluctuations [e.g., *Suzuki et al.*, 2007] and some of the nonwind effects may counteract with each other, so the task is obviously nontrivial. The statistical analysis of

Table 2. Percentage of Cases of Which the Average Value of the Absolute Ratio Between RCS Computation and GMF is Less Than 1.5 dB[a]

	DVu	DVx	DVd	DVa	DHu	DHx	DHd	DHa	DRu	DRx	DRd	DRa
Ku DU	**70.0**	**77.5**	**82.5**	**90.0**	25.0	35.0	**47.5**	32.5	30.0	32.5	60.0	35.0
Ku E	42.5	30.0	20.0	17.5	40.0	40.0	42.5	42.5	30.0	20.0	55.0	32.5
Ku H1	45.0	45.0	50.0	47.5	**50.0**	**47.5**	40.0	**50.0**	**65.0**	52.5	**85.0**	**70.0**
Ku H4	35.0	50.0	35.0	50.0	17.5	35.0	27.5	27.5	62.5	**55.0**	72.5	65.0
C DU	42.5	**47.5**	67.5	**67.5**	35.0	**47.5**	60.0	57.5	85.0	82.5	80.0	87.5
C E	**55.0**	22.5	**70.0**	60.0	47.5	35.0	**67.5**	**65.0**	**95.0**	**85.0**	**90.0**	**92.5**
C H1	**55.0**	32.5	45.0	45.0	**50.0**	25.0	22.5	22.5	72.5	80.0	82.5	80.0
C H4	35.0	45.0	42.5	40.0	42.5	**47.5**	47.5	52.5	87.5	**85.0**	85.0	**92.5**

[a]In each column, the best results for the Ku and C bands are in boldface.

Table 3. Percentage of Cases of Which the Average Value of the Absolute Ratio Between RCS Computation and GMF is Less Than 3 dB[a]

	DVu	DVx	DVd	DVa	DHu	DHx	DHd	DHa	DRu	DRx	DRd	DRa
Ku DU	**97.5**	**95.0**	**97.5**	**97.5**	52.5	60.0	**70.0**	57.5	65.0	55.0	75.0	62.5
Ku E	77.5	60.0	65.0	75.0	**75.0**	62.5	**70.0**	**75.0**	70.0	52.5	75.0	65.0
Ku H1	80.0	92.5	75.0	85.0	60.0	**70.0**	67.5	67.5	**87.5**	**75.0**	**87.5**	**87.5**
Ku H4	62.5	72.5	62.5	62.5	47.5	57.5	50.0	55.0	80.0	70.0	**87.5**	80.0
C DU	**90.0**	**92.5**	**90.0**	**95.0**	77.5	**87.5**	82.5	85.0	**100.0**	**100.0**	**100.0**	**100.0**
C E	87.5	60.0	85.0	85.0	**90.0**	70.0	**85.0**	87.5	**100.0**	**100.0**	**100.0**	**100.0**
C H1	87.5	50.0	80.0	75.0	**90.0**	47.5	67.5	**90.0**	97.5	95.0	90.0	97.5
C H4	57.5	65.0	62.5	72.5	67.5	80.0	77.5	80.0	**100.0**	**100.0**	**100.0**	**100.0**

[a]In each column, the best results for the Ku and C bands are in boldface.

Suzuki et al. [2007] as well as the simulations conducted in this paper, however, point out that the effects due to environmental variables other than mean wind speed cannot be ignored. It has been commented by *Hwang et al.* [2002, p. 1] that

> The properties of the ocean surface roughness control many dynamical and mechanical processes occurring at the air-sea interface. Examples include air-sea mass, momentum and energy exchanges and electromagnetic or acoustic wave scattering from above or below the ocean surface. In many applications, ocean surface roughness has been equated with the mean square slopes of wind waves. This concept has led to difficulties in explaining field observation of roughness related phenomena such as surface wind stress and radar scattering from the ocean surface. Due to the lack of clear understanding of ocean surface physics, in some applications the role of roughness is seriously distorted or completely ignored. For example, in the derivation of wind speed from altimeter or scatterometer output, operational algorithms rely on empirical relations established from correlating collocated and simultaneous datasets of in situ wind speeds and backscattering cross sections. The physics of wind generation of waves and scattering of radar waves from surface roughness produced by ocean wave undulation are totally avoided. With the empirical approach described above, there is little room for improvement in the accuracy of the derived geophysical parameters (e.g., wind speed from altimeter and scatterometer, salinity from microwave emission) even when major enhancements in sensor hardware and software have been implemented.

4. Summary

[28] In this paper, four different spectral functions for the ocean surface roughness are compared. The results illustrate

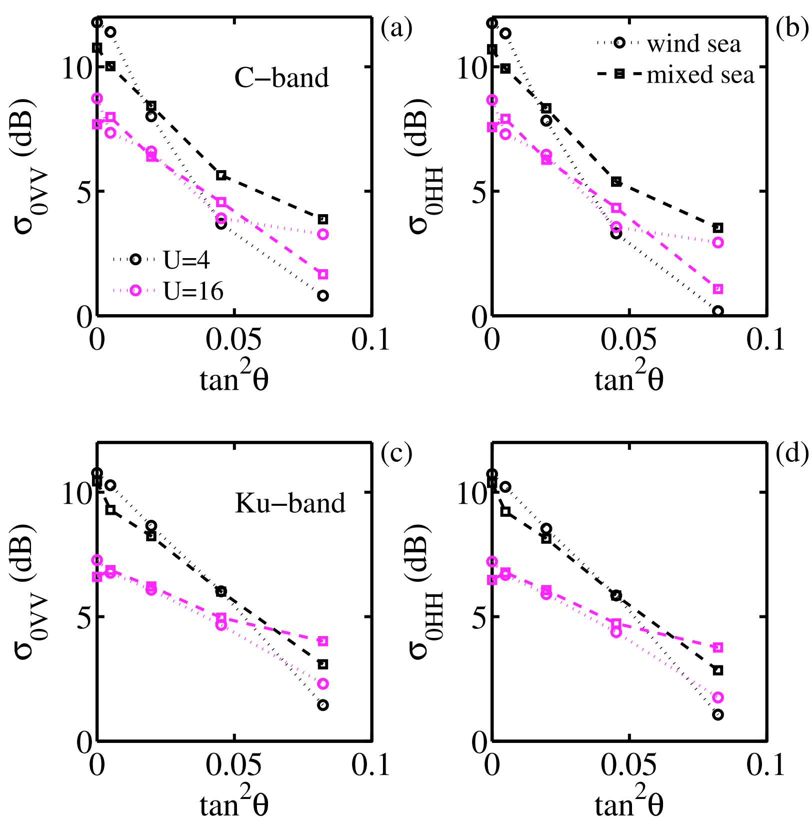

Figure 15. Examples of NRCS computations to illustrate the tilting effect of the swell component. (a) C band VV, (b) C band HH, (c) Ku band VV, and (d) Ku band HH. Circle shows wind sea, and square shows swell plus wind sea. Results for two wind speeds are shown in different colors. The horizontal coordinates of the plotting symbols correspond to θ = 0°, 4°, 8°, 12°, and 16°.

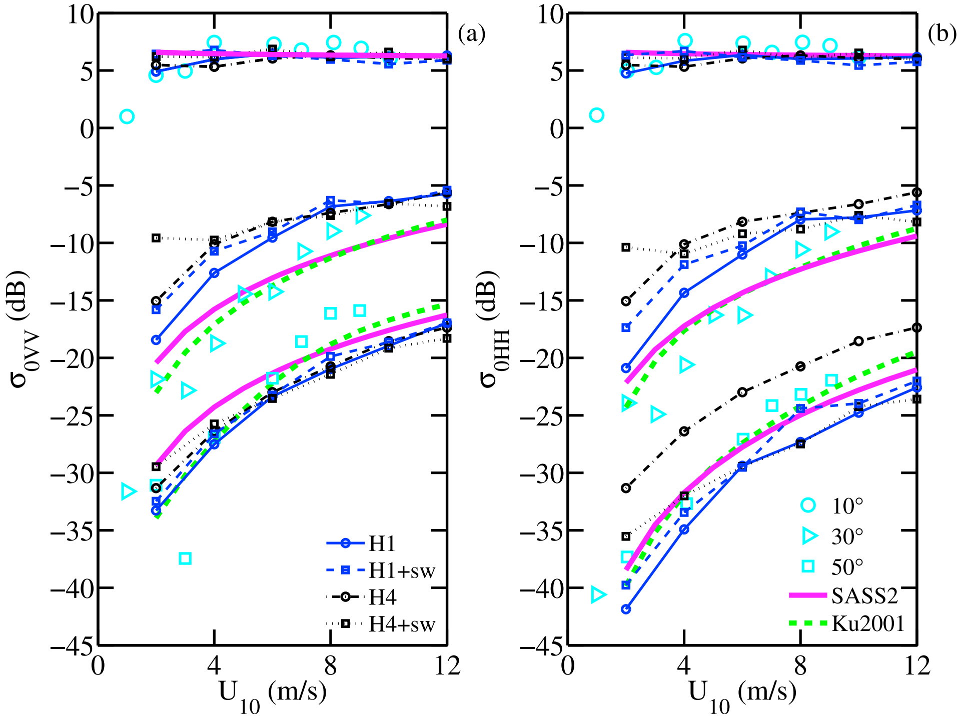

Figure 16. Examples of NRCS computations to illustrate the tilting effect of the swell component at moderate incidence angles for Ku band (a) VV and (b) HH. Experimental data of *Plant* [2002] and GMF (SASS2 and Ku2001) are shown for reference.

the significant difference in the spectral representation of the ocean surface MSS among different spectral models (Figure 1). Filtered MSS computed by integrating the wave spectra are compared to available field data obtained through remote sensing using EM frequencies ranging from optical to C band radar (Figure 2).

[29] These four roughness spectral functions are used as input for calculating the radar backscatter from the

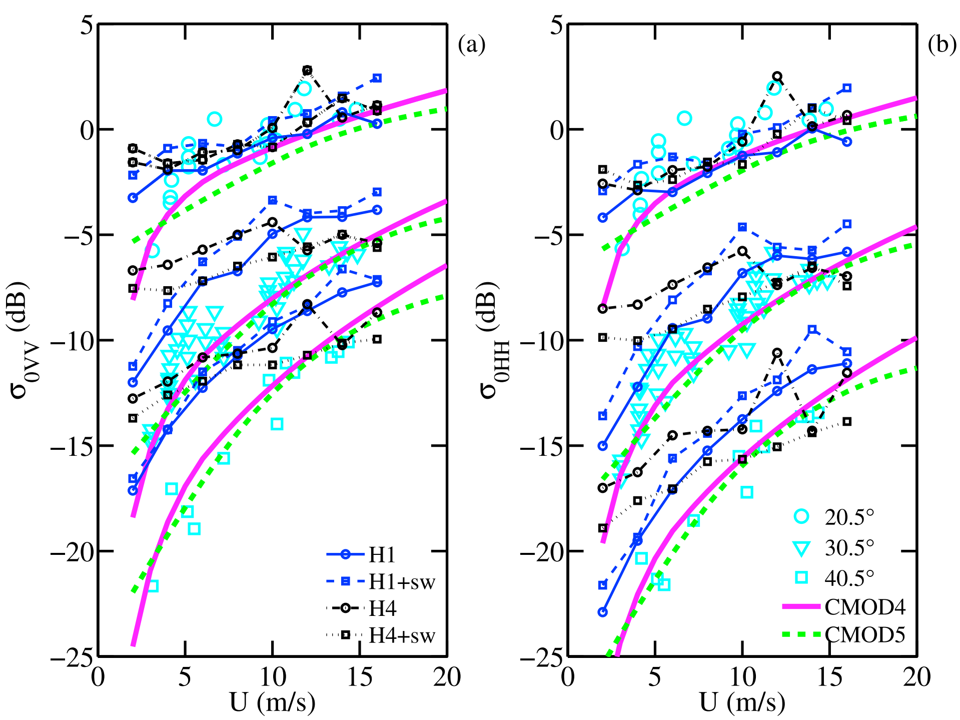

Figure 17. Same as Figure 16 for but C band. Experimental data of *Mouche et al.* [2005] and GMF (CMOD4 and CMOD5) are shown for reference.

ocean surface at various radar frequencies ranging from 1 to 18 GHz using a multiscale scattering model. The results are compared with several field data sets as well as Ku and C band GMF. The comparison results are presented side by side, both in graphic and tabulated formats (Figures 7–14 and Tables 1–3). The Ku band result is sensitive to the selected roughness spectrum. The DU spectrum performs very well for VV polarization but H1 and H4 spectra produce more even performance for VV and HH and yield better result on VV/HH polarization ratio. The C band result is much less sensitive to the choice of roughness spectrum and the agreement between NRCS computation and GMF is generally within about 3 dB for wind speed between 3 and 24 m/s and incidence angles between 20° and 60°.

[30] Effects of ocean swell include modification of the surface roughness spectrum (compare H1 and H4 spectra (Figure 1)) and directly providing tilting surfaces in addition to the longer wind generated waves. The extra tilting effect is investigated for near-nadir configuration (Figure 15) and moderate incidence angles (Figures 16 and 17). For the former, the effect is significant and may impact the accuracy of retrieving the MSS from radar measurements in near-nadir configuration. For the latter, the swell contributes to a larger variation of scatterometer measurements and modification of the wind speed dependence of the normalized radar cross section.

[31] **Acknowledgments.** This work is sponsored by the Office of Naval Research (NRL program element 62435N and 61153N and ONR grant N000140810977). We appreciate the comments from two anonymous reviewers for improving and clarifying our presentation. This is NRL contribution NRL/JA/7260-09-0169.

References

Anderson, C., T. Macklin, C. Gommenginger, M. Srokosz, J. Wolf, and J. Hargreaves (2000), Impact of sea state on nadir-looking and side-looking microwave backscatter, *Earth Obs. Q.*, *67*, 5–8. (Available at http://esapub.esrin.esa.it/eoq/eoq67/anderson.pdf.)

Banner, M. L. (1990), Equilibrium spectra of wind waves, *J. Phys. Oceanogr.*, *20*, 966–984, doi:10.1175/1520-0485(1990)020<0966:ESOWW>2.0.CO;2.

Bass, F., I. Fuks, A. Kalmykov, I. Ostrovsky, and A. Rosenberg (1968), Very high frequency radiowave scattering by a disturbed sea surface part II: Scattering from an actual sea surface, *IEEE Trans. Antennas Propag.*, *16*, 560–568, doi:10.1109/TAP.1968.1139244.

Cox, C. S., and W. Munk (1954), Statistics of the sea surface derived from Sun glitter, *J. Mar. Res.*, *13*, 198–227.

Donelan, M. A., J. Hamilton, and W. H. Hui (1985), Directional spectra of wind-generated waves, *Philos. Trans. R. Soc. London, Ser. A*, *315*, 509–562, doi:10.1098/rsta.1985.0054.

Elfouhaily, T., B. Chapron, K. Katsaros, and D. Vandemark (1997), A unified directional spectrum for long and short wind-driven waves, *J. Geophys. Res.*, *102*, 15,781–15,796, doi:10.1029/97JC00467.

Hauser, D., G. Caudal, S. Guimbard, and A. A. Mouche (2008), A study of the slope probability density function of the ocean waves from radar observations, *J. Geophys. Res.*, *113*, C02006, doi:10.1029/2007JC004264.

Hersbach, H., A. Stoffelen, and S. de Haan (2007), An improved C-band scatterometer ocean geophysical model function: CMOD5, *J. Geophys. Res.*, *112*, C03006, doi:10.1029/2006JC003743.

Hwang, P. A. (2007), Spectral signature of wave breaking in surface wave components of intermediate length scale, *J. Mar. Syst.*, *66*, 28–37, doi:10.1016/j.jmarsys.2005.11.015.

Hwang, P. A. (2008), Observations of swell influence on ocean surface roughness, *J. Geophys. Res.*, *113*, C12024, doi:10.1029/2008JC005075.

Hwang, P. A. (2009a), Estimating the effective energy transfer velocity at air-sea interface, *J. Geophys. Res.*, *114*, C11011, doi:10.1029/2009JC005497.

Hwang, P. A. (2009b), Comment on "A study of the slope probability density function of the ocean waves from radar observations" by D. Hauser et al., *J. Geophys. Res.*, *114*, C02008, doi:10.1029/2008JC005005.

Hwang, P. A., and D. W. Wang (2004), An empirical investigation of source term balance of small scale surface waves, *Geophys. Res. Lett.*, *31*, L15301, doi:10.1029/2004GL020080.

Hwang, P. A., D. W. Wang, W. J. Teague, G. A. Jacobs, J. Wesson, D. Burrage, and J. Miller (2002), Anatomy of the ocean surface roughness, *Rep. NRL/FR/7330-02-10036*, 45 pp., Nav. Res. Lab., Stennis Space Center, Miss.

Hwang, P. A., M. A. Sletten, and J. V. Toporkov (2008a), Analysis of radar sea return for breaking wave investigation, *J. Geophys. Res.*, *113*, C02003, doi:10.1029/2007JC004319.

Hwang, P. A., M. A. Sletten, and J. V. Toporkov (2008b), Breaking wave contribution to low grazing angle radar backscatter from the ocean surface, *J. Geophys. Res.*, *113*, C09017, doi:10.1029/2008JC004752.

Jackson, F. C., W. T. Walton, D. E. Hines, B. A. Walter, and C. Y. Peng (1992), Sea surface mean square slope from K_u-band backscatter data, *J. Geophys. Res.*, *97*, 11,411–11,427, doi:10.1029/92JC00766.

Jones, W., L. Schroeder, and J. Mitchell (1977), Aircraft measurements of the microwave scattering signature of the ocean, *IEEE J. Oceanic Eng.*, *2*, 52–61, doi:10.1109/JOE.1977.1145330.

Melville, W. K., R. H. Stewart, W. C. Keller, J. A. Kong, D. V. Arnold, A. T. Jessup, M. R. Loewen, and A. M. Slinn (1991), Measurements of electromagnetic bias in radar altimetry, *J. Geophys. Res.*, *96*, 4915–4924, doi:10.1029/90JC02114.

Melville, W. K., F. C. Felizardo, and P. Matusov (2004), Wave slope and wave age effects in measurements of electromagnetic bias, *J. Geophys. Res.*, *109*, C07018, doi:10.1029/2002JC001708.

Mouche, A. A., D. Hauser, J.-F. Daloze, and C. Guerin (2005), Dual-polarization measurements at C-band over the ocean: Results from airborne radar observations and comparison with ENVISAT ASAR data, *IEEE Trans. Geosci. Remote Sens.*, *43*, 753–769, doi:10.1109/TGRS.2005.843951.

Plant, W. J. (2002), A stochastic, multiscale model of microwave backscatter from the ocean, *J. Geophys. Res.*, *107*(C9), 3120, doi:10.1029/2001JC000909.

Stoffelen, A., and D. Anderson (1997), Scatterometer data interpretation: Estimation and validation of the transfer function CMOD4, *J. Geophys. Res.*, *102*, 5767–5780, doi:10.1029/96JC02860.

Suzuki, N., M. A. Donelan, and W. J. Plant (2007), On the sub-grid-scale variability of oceanic winds and the accuracy of numerical weather prediction models as deduced from QuikSCAT backscatter distributions, *J. Geophys. Res.*, *112*, C04005, doi:10.1029/2005JC003437.

Unal, C. M. H., P. Snoeij, and P. J. F. Swart (1991), The polarization-dependent relation between radar backscatter from the ocean surface and surface wind vector at frequencies between 1 and 18 GHz, *IEEE Trans. Geosci. Remote Sens.*, *29*, 621–626, doi:10.1109/36.135824.

Valenzuela, G. R. (1968), Scattering of electromagnetic waves from a tilted slightly rough surface, *Radio Sci.*, *3*, 1057–1066.

Valenzuela, G. R. (1978), Theories for the interaction of electromagnetic and oceanic waves—A review, *Boundary Layer Meteorol.*, *13*, 61–85, doi:10.1007/BF00913863.

Vandemark, D., B. Chapron, J. Sun, G. H. Crescenti, and H. C. Graber (2004), Ocean wave slope observations using radar backscatter and laser altimeters, *J. Phys. Oceanogr.*, *34*, 2825–2842, doi:10.1175/JPO2663.1.

Walsh, E. J., D. C. Vandemark, C. A. Friehe, S. P. Burns, D. Khelif, R. N. Swift, and J. F. Scott (1998), Measuring sea surface mean square slope with a 36-GHz scanning radar altimeter, *J. Geophys. Res.*, *103*, 12,587–12,601, doi:10.1029/97JC02443.

Wentz, F. J. (1977), A two scale scattering model with application to the JONSWAP '75 aircraft microwave scatterometer experiment, *NASA Contract. Rep.*, *2919*, 122 pp.

Wentz, F. J., S. Peteherych, and L. A. Thomas (1984), A model function for ocean radar cross sections at 14.6 GHz, *J. Geophys. Res.*, *89*, 3689–3704, doi:10.1029/JC089iC03p03689.

Wright, J. (1966), Backscattering from capillary waves with application to sea clutter, *IEEE Trans. Antennas Propag.*, *14*, 749–754, doi:10.1109/TAP.1966.1138799.

Wright, J. (1968), A new model for sea clutter, *IEEE Trans. Antennas Propag.*, *16*, 217–223, doi:10.1109/TAP.1968.1139147.

P. A. Hwang, Remote Sensing Division, Naval Research Laboratory, 4555 Overlook Ave. SW, Washington, DC 20375, USA. (paul.hwang@nrl.navy.mil)

W. J. Plant, Applied Physics Laboratory, University of Washington, Seattle, WA 98195, USA. (plant@apl.washington.edu)